

New constraints on the planetary system around the young active star AU Mic

Two transiting warm Neptunes near mean-motion resonance

E. Martioli^{1,2}, G. Hébrard^{1,3}, A. C. M. Correia^{4,5}, J. Laskar⁵, and A. Lecavelier des Etangs¹

¹ Institut d'Astrophysique de Paris, CNRS, UMR 7095, Sorbonne Université, 98 bis bd Arago, 75014 Paris, France, e-mail: martioli@iap.fr

² Laboratório Nacional de Astrofísica, Rua Estados Unidos 154, 37504-364, Itajubá - MG, Brazil

³ Observatoire de Haute Provence, St Michel l'Observatoire, France

⁴ CFisUC, Department of Physics, University of Coimbra, 3004-516 Coimbra, Portugal

⁵ IMCCE, UMR8028 CNRS, Observatoire de Paris, PSL University, Sorbonne Univ., 77 av. Denfert-Rochereau, 75014 Paris, France

Received December 24, 2020; accepted March 27, 2021

ABSTRACT

AU Microscopii (AU Mic) is a young, active star whose transiting planet was recently detected. Here, we report our analysis of its TESS light curve, where we modeled the BY Draconis type quasi-periodic rotational modulation by starspots simultaneously to the flaring activity and planetary transits. We measured a flare occurrence rate in AU Mic of 6.35 flares per day for flares with amplitudes in the range of $0.06\% < f_{\max} < 1.5\%$ of the star flux. We employed a Bayesian MCMC analysis to model the five transits of AU Mic b observed by TESS, improving the constraints on the planetary parameters. The measured planet-to-star effective radius ratio of $R_p/R_\star = 0.0496 \pm 0.0007$ implies a physical radius of $4.07 \pm 0.17 R_\oplus$ and a planet density of $1.4 \pm 0.4 \text{ g cm}^{-3}$, confirming that AU Mic b is a Neptune-size moderately inflated planet. While a single feature possibly due to a second planet was previously reported in the former TESS data, we report the detection of two additional transit-like events in the new TESS observations of July 2020. This represents substantial evidence for a second planet (AU Mic c) in the system. We analyzed its three available transits and obtained an orbital period of $18.859019 \pm 0.000016 \text{ d}$ and a planetary radius of $3.24 \pm 0.16 R_\oplus$, which defines AU Mic c as a warm Neptune-size planet with an expected mass in the range of $2.2 M_\oplus < M_c < 25.0 M_\oplus$, estimated from the population of exoplanets of similar sizes. The two planets in the AU Mic system are in near 9:4 mean-motion resonance. We show that this configuration is dynamically stable and should produce transit-timing variations (TTV). Our non-detection of significant TTV in AU Mic b suggests an upper limit for the mass of AU Mic c of $< 7 M_\oplus$, indicating that this planet is also likely to be inflated. As a young multi-planet system with at least two transiting planets, AU Mic becomes a key system for the study of atmospheres of infant planets and of planet-planet and planet-disk dynamics at the early stages of planetary evolution.

Key words. stars: planetary systems – stars: individual: AU Mic – stars: activity – techniques: photometric

1. Introduction

Young planetary systems represent an opportunity to observe planets in the early stages of planetary formation when gravitational interactions have not significantly changed the initial configuration of the system. AU Microscopii (AU Mic) is a particularly interesting young system, with an estimated age of $22 \pm 3 \text{ Myr}$ (Mamajek & Bell 2014), which is located at a distance of only $9.7248 \pm 0.0046 \text{ pc}$ (Gaia Collaboration 2018). Table 1 summarizes the star parameters of AU Mic that are relevant for this work. The AU Mic host is an M1 star with a spatially resolved edge-on debris disk (Kalas et al. 2004) and at least one transiting planet, AU Mic b (Plavchan et al. 2020). This Neptune-size planet is in a 8.5-d prograde orbit aligned with the stellar rotation axis (Martioli et al. 2020; Hirano et al. 2020; Palle et al. 2020). While Plavchan et al. (2020) only reported an upper limit on the mass of AU Mic b, Klein et al. (2020) measured $17.1^{+4.7}_{-4.5} M_\oplus$ thanks to infrared observations secured with the SPIRou spectropolarimeter (Donati et al. 2020). Plavchan et al. (2020) has also reported the detection of an isolated transit

event of a second possible candidate planet, hereafter referred to as AU Mic c.

The notion that AU Mic could be a host for several planets is not a surprising one. Indeed, the occurrence rate of planets with a radius between $0.5 R_\oplus$ and $4.0 R_\oplus$ and a period between 0.5 and 256 d is estimated as $8.4^{+1.2}_{-1.1}$ planets per M dwarf (Hsu et al. 2020), although the occurrence rate of more massive planets in M dwarfs decreases significantly with mass (e.g., Bonfils et al. 2013). Moreover, provided the fact that AU Mic has an edge-on debris disk and that AU Mic b is a transiting planet with an aligned orbit, the chances that other planets also reside in coplanar orbits increase and, therefore, possible close-in additional planets are also likely to transit the star.

AU Mic is a magnetically active star with strong flaring activity (Robinson et al. 2001). Its surface is largely filled by starspots, producing a BY Draconis-type light curve with a quasi-periodic rotational modulation and a period of $4.863 \pm 0.010 \text{ d}$ (Plavchan et al. 2020). As in other active stars, the strong flaring and magnetic activity of AU Mic makes it more difficult to detect planetary transits in a photometric time series, especially for small planets where the occurrence rate is higher. In

Table 1. AU Mic star parameters.

Parameter	Value	Ref.
effective temperature	3700 ± 100 K	1
star mass	$0.50 \pm 0.03 M_{\odot}$	1
star radius	$0.75 \pm 0.03 R_{\odot}$	2
rotation period	4.863 ± 0.010 d	1
age	22 ± 3 Myr	3
distance	9.7248 ± 0.0046 parsec	4
linear limb dark. coef.	0.2348	5
quadratic limb dark. coef.	0.3750	5

References. (1) Plavchan et al. (2020); (2) White et al. (2015); (3) Majek & Bell (2014); (4) Gaia Collaboration (2018); (5) Claret (2018)

this work, we present an analysis of the Transiting Exoplanet Survey Satellite (TESS) data of AU Mic, including the new observations obtained in July 2020, where we implement a multi-flare model combined with the starspots model, improving the constraints on the planetary parameters from transit modeling and allowing for the detection of two additional transits of the second candidate planet AU Mic c.

2. TESS light curve

AU Mic was observed by TESS (Ricker et al. 2015) in Sector 1 from 2018-Jul-25 to 2018-Aug-22, in cycle 1, camera 1. Then it was observed again in Sector 27 from 2020-Jul-04 to 2020-Jul-30, in cycle 3, camera 1. The second visit was observed as part of the TESS Guest Investigator Programs G03263 (PI: P. Plavchan), G03141 (PI: E. Newton), and G03273 (PI: L. Vega) in fast mode with a time sampling of 20 sec compared to the 2 min time sampling of the first visit. We obtained the de-trended photometric time series from the Mikulski Archive for Space Telescopes (MAST) using the MAST astroquery tool¹. Figure 1 shows the AU Mic PDCSAP² flux in units of electrons-per-second ($e^{-}s^{-1}$) as a function of time given in TESS Barycentric Julian Date (TBJD = BJD - 2,457,000.0) for the two visits. Plavchan et al. (2020) have analyzed the same TESS data from the first visit only, and in the present paper we report for the first time an analysis including the more recent 2020 TESS data. The predicted times of the transits of AU Mic b and c as calculated from our ephemerides (see Sects. 5 and 6) are marked with vertical lines.

3. Starspots

As illustrated in Fig. 1, the TESS light curve of AU Mic shows a typical BY Draconis type of quasi-periodic variation due to starspots modulated by stellar rotation. The starspots evolve and, therefore, this modulation cannot be accurately modeled by a single periodic function. Thus, we treat this quasi-periodic modulation as a baseline “continuum” signal, where we model it by fitting a piece-wise fourth-order polynomial with iterative sigma-clipping. This approach works well when the ranges are carefully selected and inspected as follows. First, we can be certain that the polynomial function is a sufficiently accurate approximation for the local baseline variation within each range. Then we avoid the edges of the ranges to include either a transit or a flare event. Finally, we avoid the inclusion of large gaps

¹ <https://astroquery.readthedocs.io/en/latest/mast/mast.html>

² Pre-search Data Conditioning SAP

(when TESS did not deliver data) within the same range. The edges for all selected ranges are represented by the blue vertical dashed lines in Fig. 1.

This starspot model is removed from the data to model flares and planetary transits as explained in Sects. 4, 5, and 6, which are further removed from the original data to fit the starspot modulation again. We repeat this procedure iteratively until the standard deviation of residuals is not improved by more than 1%. We typically meet this criterion upon three to five iterations. The final starspot model is also shown in Fig. 1. In Appendix A, we present an independent measurement of the rotational period of AU Mic from the starspot modulation in the 2018 TESS data.

4. Flares

AU Mic is an active young star with intense flaring activity. We carry out an analysis of the flares in the TESS data to improve the constraints on the transit events. We consider the starspot-subtracted residuals as shown in Fig. 2. The flares are typically clusters of points lying above the noise level. First we detect peaks as possible candidate flares using the `scipy.signal.find_peaks`³ routine, where it finds local maxima via a simple comparison of neighbouring values. We set a minimum peak amplitude of 2.5σ and a minimum horizontal distance between peaks of about ~ 100 minutes. Some flares in AU Mic are quite complex, while other flares occur before a previously initiated flare has ended. Therefore, we visually inspected all detected peaks to identify any possible additional peaks that have been missed by the find-peaks algorithm. After a few iterations, we identified a total of 324 flares in the whole TESS time series.

The times and amplitudes of detected peaks were adopted as initial values for the basis of performing a least-squares fit using the multi-flare model of Davenport et al. (2014), where each flare is represented by a two-phase model with a polynomial rise and an exponential decay. Figure 3 shows, as an example, the residual light curve and fit flares model for three days of flaring activity in AU Mic in both TESS visits. For each flare in the model, we fit the flare amplitude (f_{\max}), the full width at half maximum (FWHM), and the time of maximum t_{peak} . The fit parameters for all flares are presented in Appendix B.

The total continuous monitoring time of AU Mic performed by TESS was estimated as 49.75 d, where we have discounted the large gaps in the data. We detected a total of 324 flares, from which 316 have fit amplitudes above $F_{\max} > 1\sigma$, for $\sigma = 161.5 e^{-}s^{-1}$. Thus, the AU Mic global occurrence rate of flares with amplitude above $f_{\max} \gtrsim 0.06\%$ of the median stellar flux ($279544 e^{-}s^{-1}$) is estimated as 6.35 flares per day or about 1 flare every 3.8 hours. Figure 4 shows the distribution of flares as function of flare amplitudes. We fit an exponential to the measured distribution and obtained an empirical model for the occurrence rate as function of flare amplitude of $f_r = 0.17e^{-4.0f_{\max}} d^{-1}$, with f_{\max} in units of $10^2 e^{-}s^{-1}$. We notice that the strong flares, which are more important energetically, have a much lower occurrence rate and therefore a low statistical significance in our analysis. Thus, this empirical relationship is only expected to hold for flares above the detection limit imposed by the noise and for flares with a statistically significant number of events observed in the TESS data, that is, those with amplitudes in the range of $0.06\% < f_{\max} < 1.5\%$ of the star flux.

³ https://docs.scipy.org/doc/scipy/reference/generated/scipy.signal.find_peaks.html

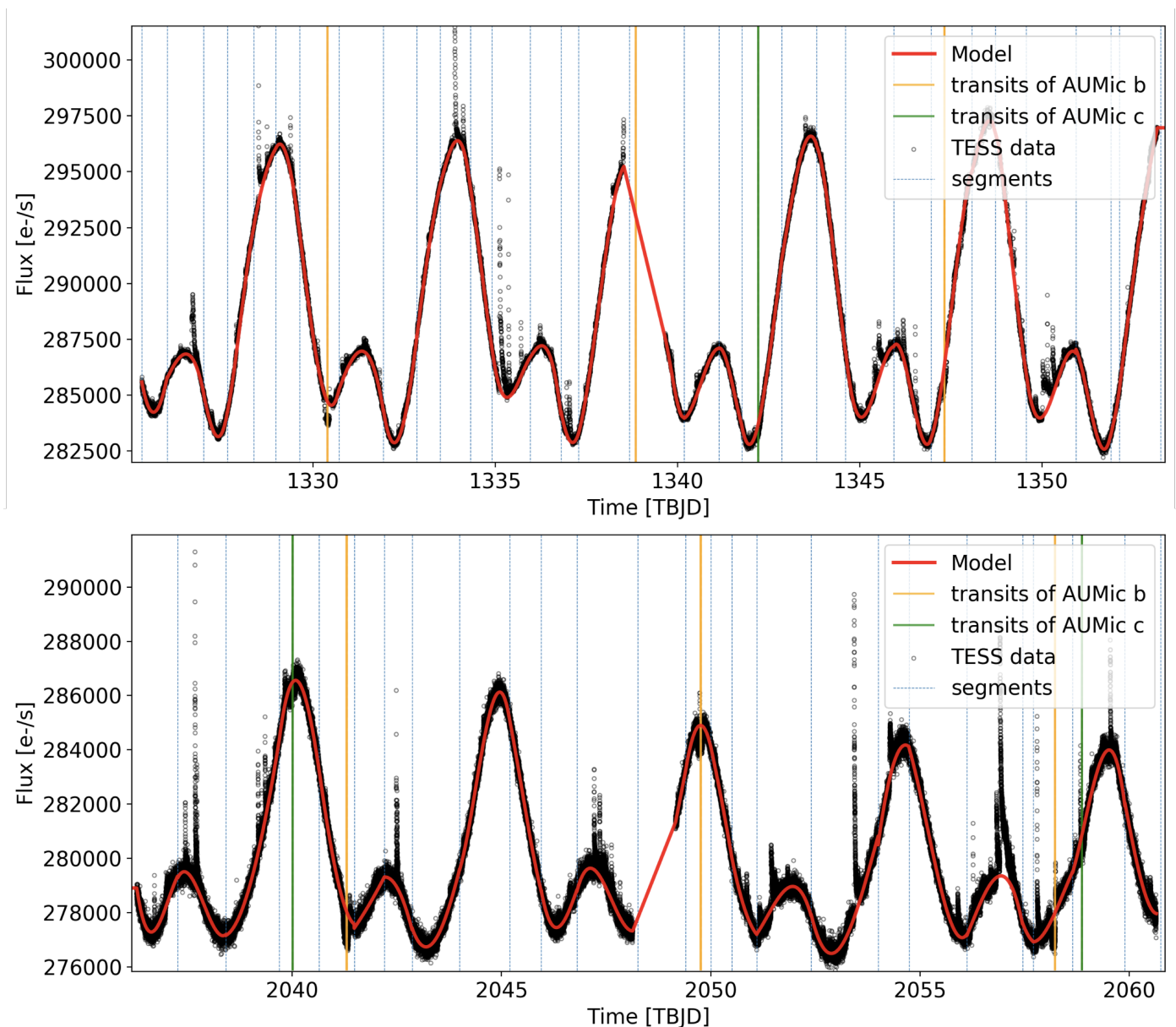


Fig. 1. TESS light curve of AU Mic. Top panel: Data for the first visit (from 2018-Jul-25 to 2018-Aug-22). Bottom panel: Data for the second visit (from 2020-Jul-04 to 2020-Jul-30). Black points are the PDCSAP flux and vertical solid lines show the times of planetary transits, as obtained in our analysis, for AU Mic b (in orange) and AU Mic c (in green). Blue vertical dashed lines show the knots of selected ranges for the piece-wise polynomial fit and the red line shows the starspot model.

The transit duration of AU Mic b calculated by Plavchan et al. (2020) is about 3.5 hours with transit depth of 0.26%. Therefore, considering that a transit observation of AU Mic b requires an out-of-transit baseline of about 2 hours, it is most likely that any transit observation in AU Mic should be affected in some way by flare events. This shows the importance of modeling flares adequately to improve the constraints on the planetary parameters obtained by the transits.

5. Transits of AU Mic b

Three transits of AU Mic b occurred during the first TESS visit, but only two have been observed due to a communication problem with the spacecraft during the second transit (see Plavchan et al. 2020). For the second visit, three other transits were expected, and indeed we were able to identify all of them. To an-

alyze these five transits together, we start with the parameters of AU Mic b from Plavchan et al. (2020), referred to as "prior values" in Table 2, to remove the transit signal from the TESS light curve before fitting the starspot and flare models. Our transit model is calculated using the BATMAN toolkit by Kreidberg (2015), where we assume a circular orbit ($e = 0$). This assumption is in agreement with Plavchan et al. (2020), who did not detect any significant eccentricity from their analysis of the transits only, where the eccentricity would be slightly constrained by the duration of the transit. We adopt as priors the quadratic limb-darkening coefficients (LDC) from Claret (2018) with an arbitrary error of 0.1, where we obtained the values calculated for the photometric system of TESS and those matching the closest stellar parameters to those of AU Mic (see Table 1).

The transits of AU Mic b, flares, and starspots are fit simultaneously using the non-linear least squares optimization (OLS)

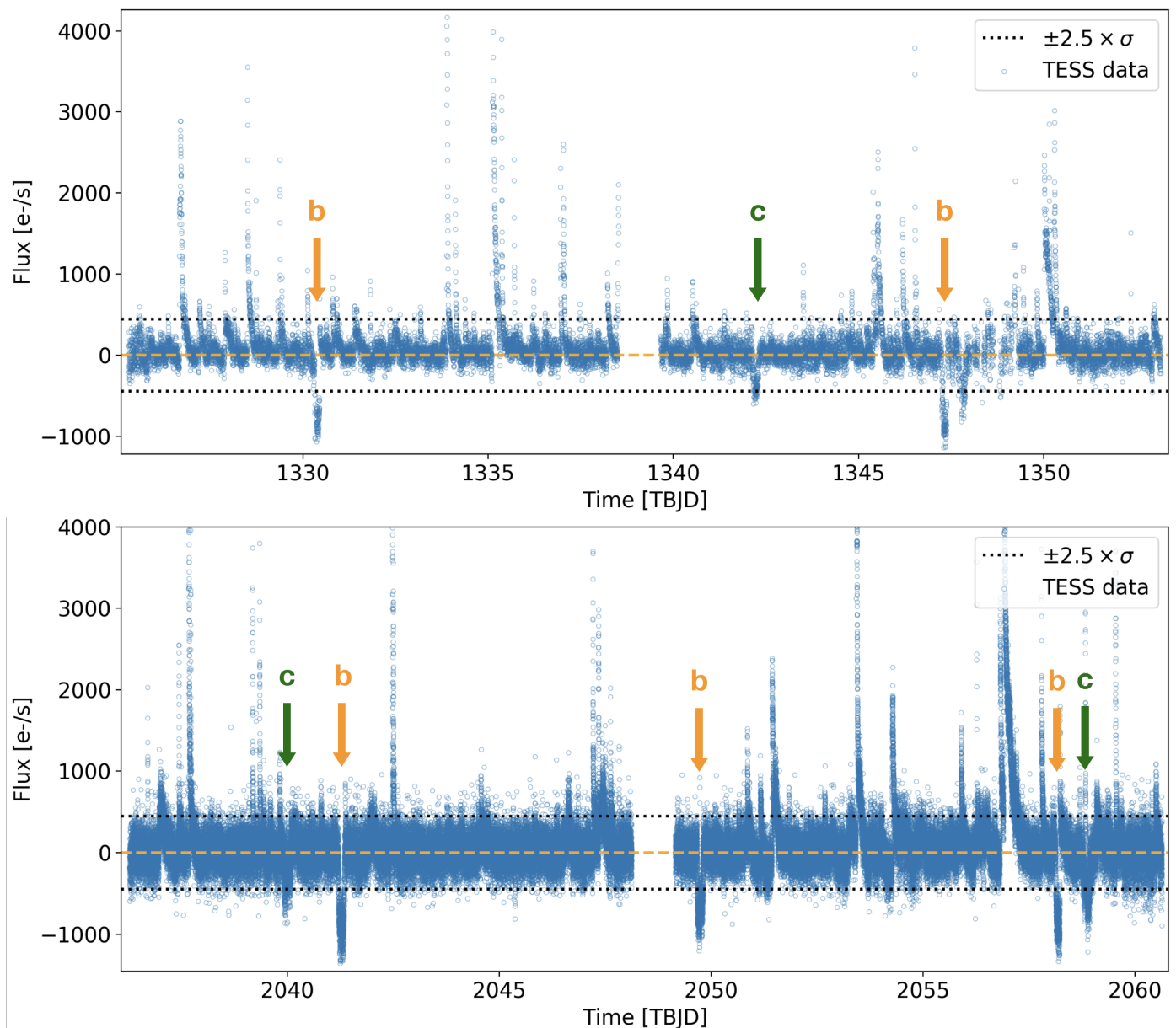


Fig. 2. TESS residual light curve of AU Mic. Top panel: Residual light curve for the first TESS visit (2018-Jul-25 to 2018-Aug-22). Bottom panel: Residual curve for the second visit (2020-Jul-04 to 2020-Jul-30). Blue circles show AU Mic TESS flux data after subtracting the starspot model and black dotted lines show $\pm 2.5\sigma$ range around the starspot fit model, for $\sigma = 162.5 \text{ e}^- \text{ s}^{-1}$. The flaring activity can be seen as positive groups of points above $+2.5\sigma$ and the transits as negative groups of points below -2.5σ . Our predicted times of transits for AU Mic b (in orange) and AU Mic c (in green) are marked with arrows.

fit tool `scipy.optimize.leastsq`. As explained in Sect. 3 this procedure is run iteratively, where we first obtain an independent fit for each component of the model and then we set these values as initial guess to run an OLS analysis with all free parameters in the three components of the model. Then we consider the data in the ranges around the transits of AU Mic b to sample the posterior distributions of the transit parameters using the `emcee` Markov chain Monte Carlo (MCMC) package (Foreman-Mackey et al. 2013). The chain is set with 100 walkers and 30000 MCMC steps of which we discard the first 5000. The MCMC samples are presented in Fig. C.1 in Appendix C, which show the chains reaching stability before the first 5000 discarded steps. The posterior distributions are illustrated in Fig. C.3 in Appendix C. The best-fit values of the transit parameters are calculated as

the medians of the posterior distribution with error bars defined by the 34% on each side of the median, all presented in Table 2.

Figure 5 shows the results of our analysis for each transit range separately, and the bottom right panel shows the flux normalized by the starspot and flare models for all transits together, and our best fit model along with the previous model of Plavchan et al. (2020) for comparison. The dispersion of residuals are 358, 433, 633, 566, and 588 ppm, for each respective epoch. The global dispersion is 573 ppm. Notice that our measured parameters of AU Mic b agree within 3σ with the previous measurements by Plavchan et al. (2020) but with improved accuracy. Our measured planet-to-star radius ratio is slightly larger than that measured by Plavchan et al. (2020) (see lower, right panel of Fig. 5). However, as described in Sect. 7, our derived effective

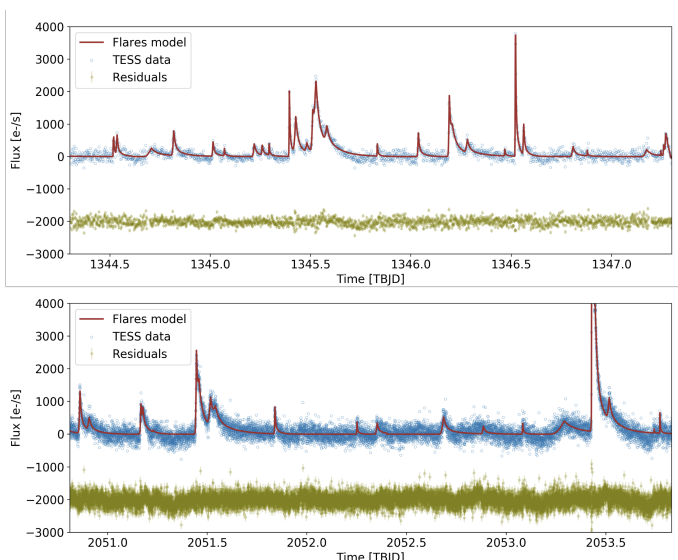


Fig. 3. TESS residual light curve of AU Mic between TBJD=1344.3 and TBJD=1347.3 (top panel) and between TBJD=2050.8 and TBJD=2053.8 (bottom panel). Blue circles show the flux after subtracting the starspot model, brown line shows the multi-flare best fit model. Green points show the residuals with an arbitrary offset for better visualization. The dispersion of residuals are $107 \text{ e}^- \text{ s}^{-1}$ and $178 \text{ e}^- \text{ s}^{-1}$ for data presented in top panel and bottom panel, respectively.

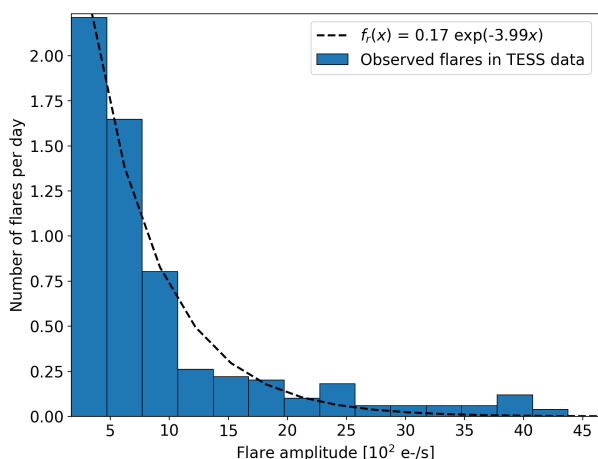


Fig. 4. Number of flares normalized by the total observed time of 49.75 d as function of flare amplitude. Dashed line shows the fit to an exponential decay as shown in the legend, where variable x represents the flare amplitude.

planetary radius of $1.05 \pm 0.04 R_{\text{Nep}}$ is slightly smaller than the value $1.08 \pm 0.05 R_{\text{Nep}}$ reported by Plavchan et al. (2020).

6. Confirmation and characterization of planet AU Mic c

An isolated candidate transit event at $T_c = 1342.22 \pm 0.03$ TBJD was identified in the 2018 TESS data by Plavchan et al. (2020), which was interpreted as a possible second planet in a 30 ± 6 -d orbit. We have searched for other transit-like events in the TESS data by looking at regions with systematic flux dips below the noise level. We identified three regions as potential transits including the one previously identified by Plavchan et al. (2020)

(see Fig. 2). We notice that there is an additional region presenting a significant flux dip around TBJD = 1347.8, which did not include as a possible transit. The 2018 TESS data after TBJD ~ 1347.7 contain several gaps, which have an impact on the modeling of the baseline modulation by starspots as well as on the detection and modeling of flares. Therefore, we presume that the apparent flux dip in this region is more likely due to a misfit other than a transit. In addition the shape of that dip is different from that of the three features above.

We hypothesize that the three selected events are transits of the same candidate planet AU Mic c. In order to test this hypothesis, we first obtain an orbital period that is consistent with the three transits, that is, a period given by the slope of a linear fit to the ephemeris equation, $T_c = T_0 + P \times E$, with T_c as the times of conjunction measured independently for each event and E as the corresponding epochs to each event, assumed to be 0, 37, and 38. We find an orbital period of $P = 18.85895 \pm 0.00003$ d. However, we note that with this particular periodicity, only three events would occur during the TESS observations (see Fig. 1). The possibility of shorter alias periods is ruled out by the fact that TESS would have observed more transits of this object and we did not detect them. To test further our hypothesis, we performed an independent analysis of each event assuming an orbital period, first with an uniform prior of $P = \mathcal{U}(1, 500)$ d to explore a broad range of periods, and then with a normal prior of $P = \mathcal{N}(18.86, 0.01)$ d, which explores a solution constrained by the previous knowledge imposed by our hypothesis. Analogously, the normalized semi-major axes are also first set with an uniform prior of $a/R_\star = \mathcal{U}(1, 500)$ and then with a normal prior estimated using the Kepler's law, that is, $a/R_\star = \mathcal{N}(31.5, 1.4)$. The priors for the times of conjunction are measured locally on each event, for example, for the first event, we obtained $T_0 = \mathcal{N}(1342.23, 0.01)$. The prior for the planet-to-star radius ratio is estimated from the square root of the average flux depth of the three events, assuming a conservative error, that is, $R_p/R_\star = \mathcal{N}(0.04, 0.01)$. The orbital inclination is considered with an uniform prior distribution of $i = \mathcal{U}(85^\circ, 90^\circ)$ and the limb darkening coefficients are fixed to the literature values presented in Table 1. In Appendix D, we present the results for this independent analysis of each transit. The posterior of all the transit parameters agree within 3σ (see Table D.1), and the dispersion of residuals improves when we adopted the fit period of $P = \mathcal{N}(18.86, 0.01)$ d as prior, which supports our hypothesis that these three events were caused by the transits of the same planet AU Mic c. Finally, we perform a joint analysis of the three transits simultaneously, where we adopt the same priors as in the independent analysis above, except for the limb darkening coefficients, where we adopted a normal prior with the literature values and an arbitrary error of 1.0. We call attention to the fact that the limb darkening coefficients obtained in Sect. 5 could have been used as priors since both planets are transiting the same star. However, the two planets may transit the stellar disk in different regions, and since AU Mic is largely filled by starspots, the limb darkening may also be affected by the different temperatures of the transited regions in the photosphere. Table 3 presents the priors and fit parameters, while Fig. 6 shows the TESS data for the three transits and the best-fit model obtained from our analysis. As in Sect. 5, the MCMC samples and posterior distributions are illustrated in Figs. C.2 and C.4 in Appendix C.

7. Discussion

We combine the transit parameters of AU Mic b and c presented in Tables 2 and 3 with the star parameters from Table 1 to cal-

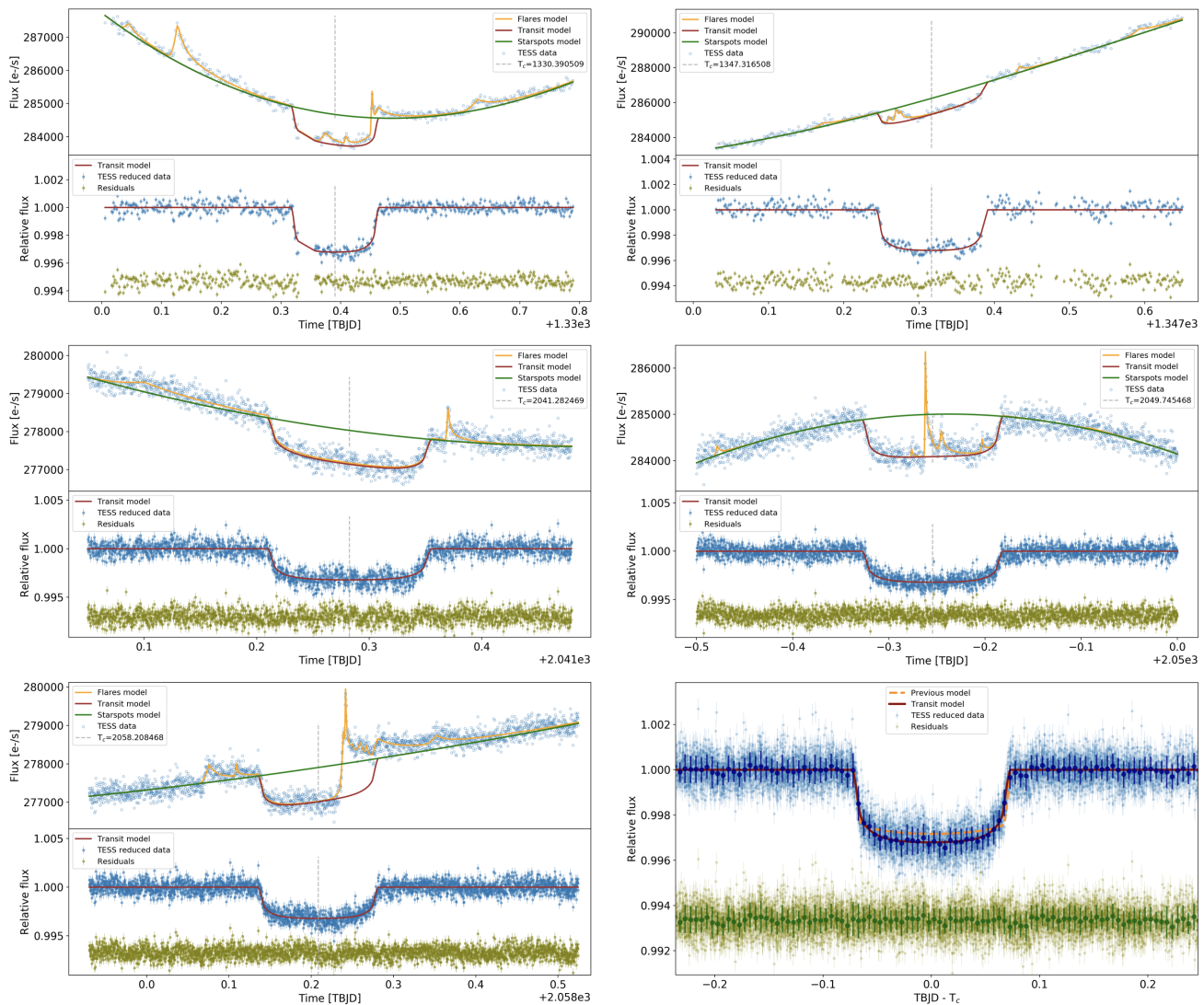


Fig. 5. Each panel shows the range around one of the five transits of AU Mic b observed by TESS. The top part of each panel shows the TESS data (blue circles) and the best-fit model for each component, as indicated in the legend. The bottom part in each panel shows the TESS data normalized by the starspot and flare model (blue points) and the best-fit transit model (red line). Vertical dashed lines show the central time of each transit. The bottom right panel shows the phase-folded light curve for all the data from the five transits (light blue points) and the binned data (dark blue points) with a bin size of 0.005 d, our best fit model (red line), and the previous fit model of Plavchan et al. (2020) for comparison (orange dashed line). The residuals (green points) are displayed with an arbitrary offset.

culate a number of derived parameters, which are presented in Table 4.

The planet-to-star radius ratio obtained in Sects. 5 and 6 are likely overestimated due to the presence of spots covering a significant fraction of the stellar photosphere. This is because the observed transit depth is likely smaller than the nominal depth that would be obtained for a completely unspotted photosphere. Therefore, an effective planet-to-star radius ratio can be obtained by applying a correction factor to the observed transit depth as in Eq. 1 of Rackham et al. (2018), that is,

$$\left(\frac{R_p}{R_\star}\right)_{\text{eff}}^2 = \left[1 - f_{\text{spot}} \left(1 - \frac{F_{\text{spot}}}{F_{\text{phot}}}\right)\right] \left(\frac{R_p}{R_\star}\right)_{\text{obs}}^2 \quad (1)$$

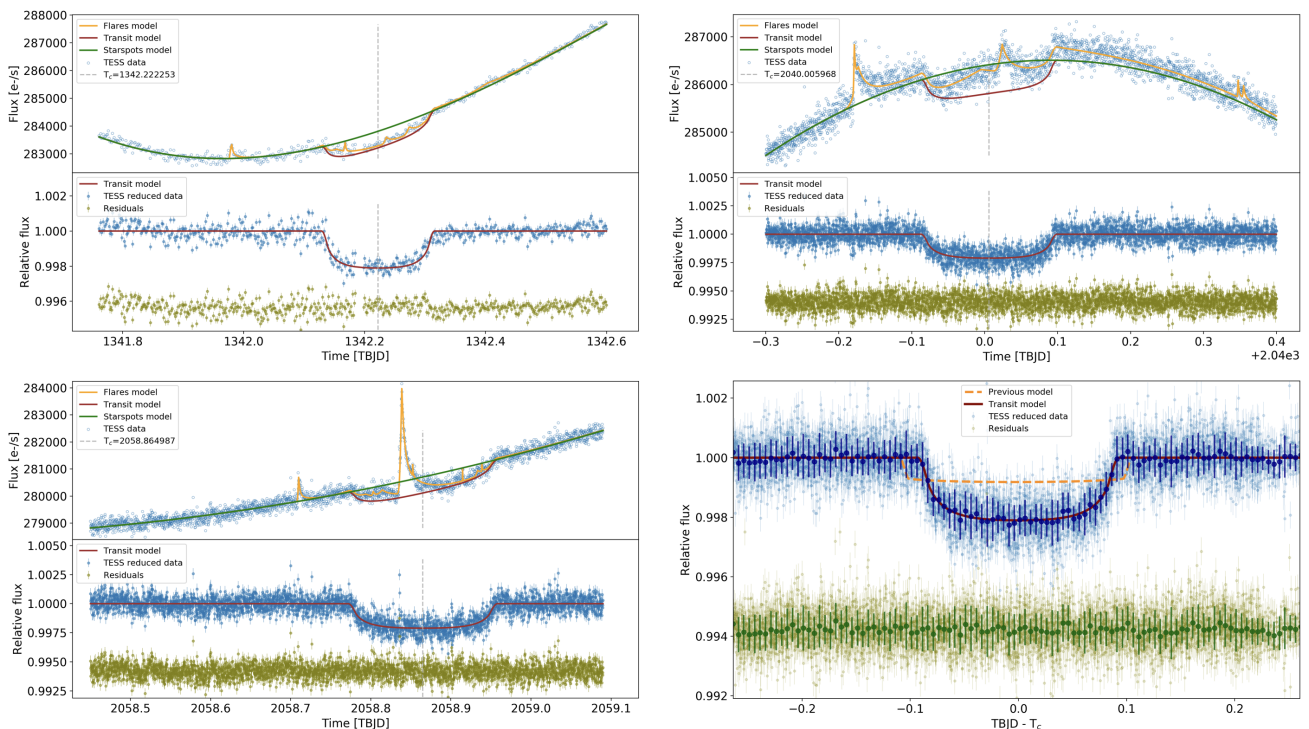
for f_{spot} being the spot filling factor estimated at 20% based on magnetic activity (Klein et al. 2020) and $F_{\text{spot}}/F_{\text{phot}}$ being the flux fraction between the spots and the photosphere. The

latter can be estimated assuming a blackbody flux for each of the two components, where the photospheric temperature is $T_{\text{phot}} = 3700$ K and the spots' temperature is estimated at 86% of the photospheric value in M1 stars (Rackham et al. 2018). The latter is in agreement with spectropolarimetric measurements of AU Mic by Berdyugina (2011). Our estimation for the spot-to-photosphere flux fraction integrated over the TESS band pass (between 600 nm and 1000 nm) is $F_{\text{spot}}/F_{\text{phot}} \sim 46\%$. Therefore, the effective radius for both transiting planets in the AU Mic system should be given by $R_p^{\text{eff}} = 0.94R_p^{\text{obs}}$, that is, about 6% smaller than the measured radius.

In addition to the correction above, there is an uncertainty in the planet radius due to the rotational modulation by starspots and other photospheric heterogeneities, which implies a variable baseline flux. To account for this additional uncertainty, we considered the amplitude of the photospheric modulation in the AU Mic TESS light curve, which is about 5%. This variability

Table 2. Transit fit parameters for planet AU Mic b obtained in our analysis from a simultaneous fit of the five transits observed by TESS as illustrated in Figs. 5 and C.3.

Parameter	Prior value	MCMC fit value
time of conjunction, T_0 [TBJD]	$1330.38957^{+0.00015}_{-0.00068}$	1330.39051 ± 0.00015
orbital period, P [d]	8.46321 ± 0.00004	8.463000 ± 0.000002
normalized semi-major axis, a/R_\star	$19.1^{+1.8}_{-1.6}$	$19.1^{+0.2}_{-0.4}$
orbital inclination, i [degree]	89.5 ± 0.4	$89.5^{+0.4}_{-0.3}$
planet-to-star radius ratio, R_p/R_\star	0.0514 ± 0.0013	$0.0526^{+0.0003}_{-0.0002}$
linear limb dark. coef., u_0	$\mathcal{N}(0.23, 0.1)$	0.13 ± 0.03
quadratic limb dark. coef., u_1	$\mathcal{N}(0.38, 0.1)$	0.58 ± 0.06


Fig. 6. Each panel shows the range around one of the five transits of AU Mic b observed by TESS. Details are the same as in Fig. 5, but here we present the results for the three TESS transits of AU Mic c. The dispersion of residuals are 370, 646, 609 ppm, for each respective epoch. The global dispersion is 609 ppm.

propagates an uncertainty on the order of $\sim \sqrt{0.05}$ to the planet radius measurements, which is included in the uncertainty values reported in Table 4.

Klein et al. (2020) recently measured a semi-amplitude of the radial velocity of the reflex motion caused by AU Mic b of $K_b = 8.5^{+2.3}_{-2.2} \text{ m s}^{-1}$, providing an important constraint on the mass of this planet. We recalculated the planet density based on our radius measurement and obtained $\rho_b = 1.4 \pm 0.4 \text{ g cm}^{-3}$.

To estimate a plausible mass range for AU Mic c, we considered a population of transiting exoplanets⁴ with radii within 1σ of the measured radius of AU Mic c, as presented in Fig. 7. The median and median absolute deviation of the mass of exoplanets in this population is $0.043 \pm 0.036 M_{\text{Jup}}$. Therefore, the mass of AU Mic c is likely to lie in the range of $0.007 M_{\text{Jup}} < M_c < 0.079 M_{\text{Jup}}$, implying a planet density in the range of

$0.4 \text{ g cm}^{-3} < \rho_c < 4.1 \text{ g cm}^{-3}$. Several different scenarios are possible for the internal structure of this planet depending on its mass. We estimate the semi-amplitude of the induced radial velocity caused by AU Mic c in the star motion to be in the range of $0.8 \text{ m s}^{-1} < K_c < 9.5 \text{ m s}^{-1}$. A number of world-class spectrometers can currently achieve the necessary precision to detect such reflex motion. However, the intense stellar activity in AU Mic may represent a challenge for such measurement.

In order to analyze the stability of the orbital solution (Table 4), we performed a global frequency analysis (Laskar 1990, 1993) in the vicinity of the best fit, in the same way as achieved for other planetary systems (e.g., Correia et al. 2005, 2010). The system is integrated on a regular 2D mesh of initial conditions, with varying semi-major axis and eccentricity of planet c, while the other parameters are retained at their nominal values. We used the symplectic integrator SABA1064 of Farrés et al. (2013), with a step size of $5 \times 10^{-3} \text{ yr}$ and general relativity corrections.

⁴ exoplanet parameters compiled from exoplanet.eu

Table 3. Transit fit parameters for planet AU Mic c obtained in our analysis from a simultaneous fit of the three transits observed by TESS as illustrated in Figs. 6 and C.4.

Parameter	Prior value	MCMC fit value
time of conjunction, T_0 [TBJD]	$\mathcal{N}(1342.23, 0.01)$	1342.2223 ± 0.0005
orbital period, P [d]	$\mathcal{N}(18.86, 0.01)$	$18.859019^{+0.000016}_{-0.000015}$
normalized semi-major axis, a/R_\star	$\mathcal{N}(31.5, 1.4)$	29 ± 3
orbital inclination, i [degree]	$\mathcal{U}(85, 90)$	$89.0^{+0.5}_{-0.4}$
planet-to-star radius ratio, R_p/R_\star	$\mathcal{N}(0.04, 0.01)$	$0.0418^{+0.0010}_{-0.0012}$
linear limb dark. coef., u_0	$\mathcal{N}(0.23, 1.0)$	$0.0^{+0.2}_{-0.3}$
quadratic limb dark. coef., u_1	$\mathcal{N}(0.38, 1.0)$	$1.2^{+0.4}_{-0.3}$

Table 4. Summary of the parameters of planets AU Mic b and AU Mic c.

Parameter	unit	AU Mic b	AU Mic c
time of conjunction	TBJD	1330.39051 ± 0.00015	1342.2223 ± 0.0005
orbital period	d	8.463000 ± 0.000002	18.859019 ± 0.000016
normalized semi-major axis, a/R_\star	-	19.1 ± 0.3	29 ± 3
semi-major axis †	au	0.0645 ± 0.0013	0.1101 ± 0.0022
transit duration	h	3.50 ± 0.08	4.5 ± 0.8
orbital inclination	degree	89.5 ± 0.3	$89.0^{+0.5}_{-0.4}$
impact parameter	R_\star	0.18 ± 0.11	0.51 ± 0.21
eccentricity	-	0 (FIXED)	0 (FIXED)
planet-to-star radius ratio § , R_p/R_\star	-	0.0496 ± 0.0007	0.0395 ± 0.0011
planet radius	R_{Jup}	0.371 ± 0.016	0.295 ± 0.014
planet radius	R_{Nep}	1.05 ± 0.04	0.84 ± 0.04
planet radius	R_\oplus	4.07 ± 0.17	3.24 ± 0.16
velocity semi-amplitude	m s^{-1}	$8.5^{+2.3}_{-2.2}$ §§	$0.8 < K_c < 9.5$
planet mass	M_{Jup}	0.054 ± 0.015 §§	$0.007 < M_c < 0.079$
planet mass	M_{Nep}	1.00 ± 0.27 §§	$0.13 < M_c < 1.46$
planet mass	M_\oplus	17 ± 5 §§	$2.2 < M_c < 25.0$
planet density	g cm^{-3}	1.4 ± 0.4	$0.4 < \rho_c < 4.1$
equilibrium temperature	K	593 ± 21	454 ± 16

References. † semi-major axis derived from the fit period and the Kepler’s law; § radius values correspond to the effective radius, which is already corrected for spot coverage and contains an additional uncertainty due to rotational modulation, as explained in Sect. 7; §§ Klein et al. (2020)

Each initial condition is integrated over 5 kyr, and a stability indicator is computed to be the variation in the measured mean motion over the two consecutive 2.5 kyr intervals of time (for more details see Couetdic et al. 2010). For regular motion, there is no significant variation in the mean motion along the trajectory, while it can vary significantly for chaotic trajectories.

In Fig. 8, we show the wide vicinity of the nominal solution for two different configurations, one with $M_c = 25.0 M_\oplus$ (top) and another with $M_c = 2.2 M_\oplus$ (bottom), corresponding to the maximum and minimum masses of the outer planet, respectively. The stability indicator is reported using a color index, where “red” represents the strongly chaotic trajectories and “dark-blue” shows the extremely stable ones. We observe that there are several islands of mean motion resonances nearby, however, the main difference is that when the mass of the outer planet is large, these resonances become unstable. The best fit nominal solution (vertical dotted line) is close to the 9:4 resonance, but outside, and so the nominal solution is in the stable zone for both mass values, as long as $e_c < 0.2$. We hence conclude that the AU Mic planetary system is stable and nearly circular.

The proximity to the 9:4 resonance could cause significant transit-timing variation (TTV). To measure the TTV for both planets, we run an MCMC analysis for each individual transit observed by TESS, where we obtained an independent measurement of the times of transits. The transit parameters are fixed to their best fit values, except T_c , which is set with a uniform prior distribution of $\mathcal{U}(T_c - 0.005, T_c + 0.005)$, for T_c being the time of conjunction calculated from the fit ephemeris. We subtract T_c from the measured times of conjunction to obtain the TTVs as presented in Table 5. We detect no significant TTV in the TESS data. TTVs with amplitudes of one minute or more would have been likely detected in this dataset.

Using the nominal solution from Table 4, we generated the synthetic TTVs as in Hébrard et al. (2020), for the minimum and the maximum masses of the outer planet. In Fig. 9, we show the variations corresponding to each solution superimposed with the observational data (Table 5). For the outer planet, the amplitude of the TTV is around one minute for both mass choices. However, for the inner planet, the minimum mass produces TTV with an amplitude of only a few seconds, while for the maximum

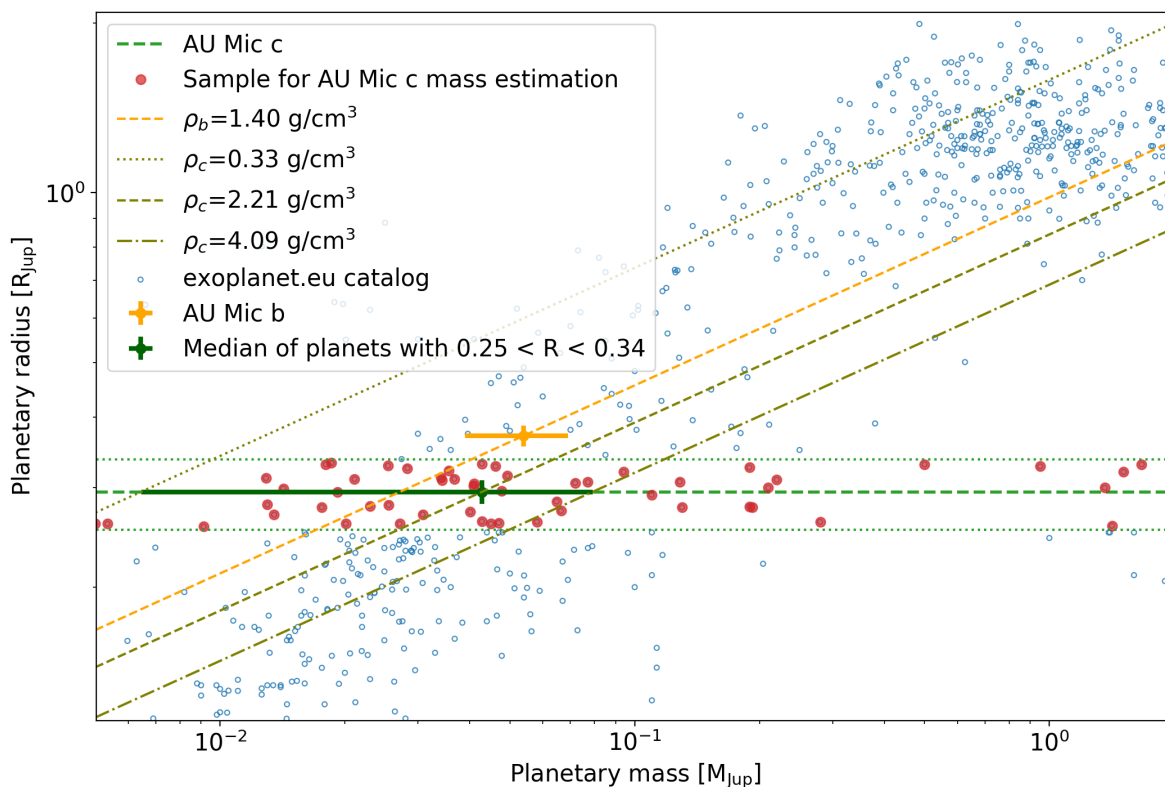


Fig. 7. Mass-radius diagram of planets. Blue circles show the known transiting exoplanets compiled from *exoplanet.eu*. The orange point represents AU Mic b and the light green horizontal dashed and dotted lines represent the AU Mic c radius measurement and $\pm 1\sigma$ uncertainties. Dark green point represents the median of planets with radius within 1σ of the measured radius of AU Mic c. Dashed orange line shows an iso-density line for the radius and mass of AU Mic b and the olive lines correspond to the iso-densities obtained for the radius of AU Mic c and for the lower limit (dotted), median value (dashed), and upper limit (dot-dashed) of the mass of AU Mic c, based on the exoplanet population with the same radii.

Table 5. Measurements of the transit-timing variation (TTV) for the transits of AU Mic b and c observed by TESS.

Planet	epoch	T_c (TBJD)	TTV (s)
b	0	1330.39046 ± 0.00016	-32 ± 17
b	2	1347.31646 ± 0.00016	$+39 \pm 21$
b	84	2041.28238 ± 0.00026	-41 ± 25
b	85	2049.74538 ± 0.00026	$+31 \pm 32$
b	86	2058.20838 ± 0.00026	$+27 \pm 27$
c	0	1342.22432 ± 0.00031	-13 ± 43
c	37	2040.00697 ± 0.00048	-81 ± 53
c	38	2058.86596 ± 0.00049	$+92 \pm 59$

mass the amplitude can reach up to three minutes. Thus, the TTV of the inner planet can place constraints on the mass of the outer planet.

The precision and the number of photometric measurements currently available for the AU Mic system (Table 5) do not allow us to run an exhaustive search for a best fit solution, but they allow us to reduce the uncertainty in the mass of the outer planet. The non-detection of TTVs that are larger than one minute place the mass of the outer planet on the low side as the likelier assumption. In Fig. 9, we show the TTV corresponding to an outer companion with $M_c = 7.0 M_\oplus$. This mass generates TTVs with

an amplitude around one minute corresponding to our upper limit. The observation of additional transits should help to resolve the present ambiguity in the outer planet mass.

Furthermore, we calculated the habitable zone (HZ) for AU Mic using the equations and data from Kopparapu et al. (2014), which gives an optimistic lower limit (recent Venus) at 0.25 au, and an upper limit (early Mars) at 0.64 au, with the runaway greenhouse limits ($M_p = 1 M_\oplus$) ranging between 0.32 au and 0.61 au. AU Mic b and c being at an orbital distance of 0.0645 ± 0.0013 au and 0.1101 ± 0.0022 au are not in the HZ. We estimate the equilibrium temperatures as in Heng & Demory (2013) assuming a uniform heat redistribution and an arbitrary geometric albedo of 0.1, which gives $T_{\text{eq,b}} = 593 \pm 21$ K and $T_{\text{eq,c}} = 454 \pm 16$ K, for AU Mic b and c, respectively, showing that these warm Neptunes are indeed too hot to sustain water in liquid state. Moreover, the actual temperature for these planets could be much higher due to a possible greenhouse effect depending on their atmospheric composition and also due to an elevated internal temperature provided the young age of the system.

8. Conclusions

We presented an analysis of the photometric TESS observations of the active young M1 star AU Mic, where we model the rota-

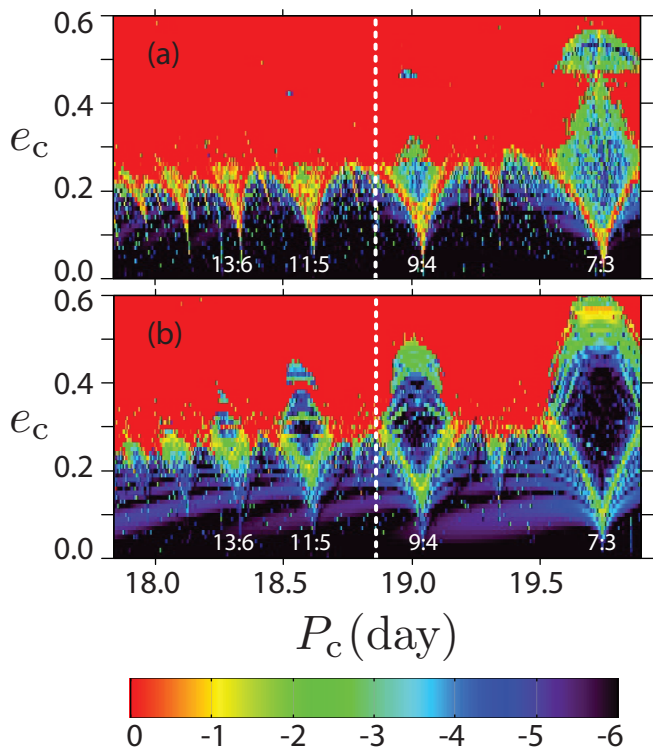


Fig. 8. Stability analysis of the AU Mic planetary system, around the best fit solution (Table 4), with $M_c = 25.0 M_{\oplus}$ (a), and $M_c = 2.2 M_{\oplus}$ (b). The phase space of the system is explored by varying the semi-major axis a_c (and thus the period P_c) and eccentricity e_c of the outer planet; e_c is plotted as a function of P_c and not a_c , as the uncertainty on a_c is larger. For the initial conditions, the step size is 0.01 in eccentricity, and 2×10^{-5} au in semi-major axis. For each initial condition, the system is integrated over 5 kyr and a stability criterion is derived with the frequency analysis of the mean longitude. The chaotic diffusion is measured by the variation in the mean motion. The color scale corresponds to the decimal logarithm of the variation of the mean motion (Correia et al. 2010). The “red” zone corresponds to highly unstable orbits, while the “dark-blue” region can be assumed to be stable on a billion-years timescale. The main resonances in the vicinity of the solution (13:6, 11:5, 9:4, 7:3) are labeled. It should be noted that for the lower value of the mass M_c (b), the libration island is mostly stable while it is not the case for the larger value of M_c (a).

tional modulation by starspots, the flaring activity, and the planetary transits simultaneously. Our analysis delivered an estimation of the flare occurrence rate of 6.35 flares per day for flares with amplitudes in the range of $0.06\% < f_{\max} < 1.5\%$ of the star flux. With such a flare rate it is important to model flaring activity to improve the constraints on the planetary parameters from transits. In our simple multi-flare model, we did not explore a detailed physical modeling of flares (e.g., as in Tilley et al. 2019) that could, in principle, be studied more extensively given the high quality and broad time coverage of these TESS observations. Our aim was to find an empirical description of flares that improves the constraints on the planetary parameters of AU Mic b and that increases the sensitivity for detecting and characterizing the second planet AU Mic c.

Our analysis of the five transits of AU Mic b provided measurements of the orbital period and time of conjunction, giving an improved ephemeris of $T_c = 2458330.39051 \pm 0.00015 + E \times 8.463000 \pm 0.000002$ JD for an accurate prediction of the times of future transits. Our detection of two new transits in the recent TESS observations have provided substantial evidence

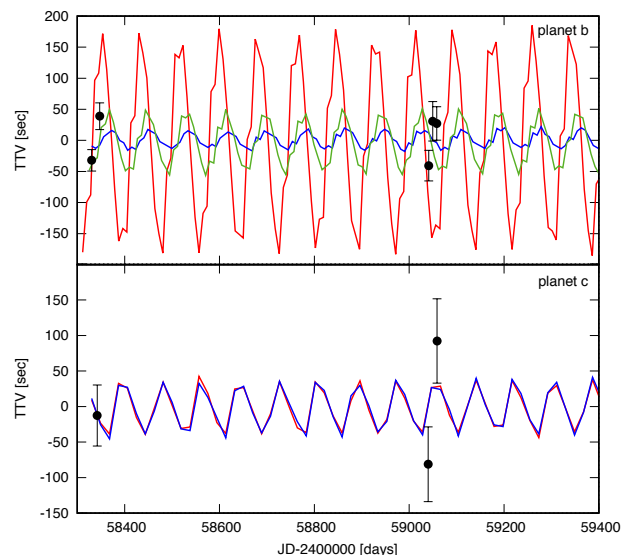


Fig. 9. Transit timing variations for AU Mic b (top) and AU Mic c (bottom). The colored lines correspond to synthetic data obtained with the best fit solution (Table 4) using different values for the mass of the outer planet: $M_c = 2.2 M_{\oplus}$ (blue), $M_c = 7.0 M_{\oplus}$ (green), and $M_c = 25.0 M_{\oplus}$ (red). The dots correspond to the observed TTVs. (Table 5).

to confirm the second planet, that is, AU Mic c. We analyzed the three transits and obtained consistent results for the planetary parameters, which supports our hypothesis that these transits come from the same planet. Our MCMC analysis provided a determination of the planetary parameters for AU Mic c, delivering an ephemeris of $T_c = 2458342.2223 \pm 0.0005 + E \times 18.859019^{+0.000016}_{-0.000015}$ JD for the times of transits with a transit duration of 4.5 ± 0.8 hours. The derived radius of $3.24 \pm 0.16 R_{\oplus}$ indicates that AU Mic c is a Neptune-size planet with an expected mass in the range of $2.2 M_{\oplus} < M_c < 25.0 M_{\oplus}$, estimated from the population of exoplanets of a similar size.

AU Mic b and c with an orbital period of 8.46 d and 18.86 d are near the 9:4 mean-motion resonance. Such a configuration is stable and could cause significant TTV, which we do not detect with the current dataset. Still, that non-detection provides an upper limit to the mass of AU Mic c of $M_c < 7 M_{\oplus}$, implying an upper limit to the planet density of $\rho_c < 1.3 \text{ g cm}^{-3}$. This suggests that both planets are likely inflated, as it should be expected for young planets (e.g., Helled et al. 2020). Therefore, these planets are interesting targets for atmospheric characterization by transmission spectroscopy.

The interactions between the planets coupled in a near 9:4 mean-motion resonance and the debris disk surrounding the star are to be the subject of subsequent studies. High-resolution images have revealed that the disk has a complex structure with small-sized substructures, such as “feature A” at a dozen astronomical units showing a “loop-like” morphology (Wisniewski et al. 2019). As for the case of β Pictoris, it has been shown that the planets can sculpt the disk morphology through the gravitational interaction between planets and the debris disk parents bodies at far distances (Lecavelier Des Etangs et al. 1996; Augereau et al. 2001), particularly through resonance mechanisms in young systems that are still evolving (Lecavelier Des Etangs 1998). The impact of the presence of AU Mic b and AU Mic c on the dust disk deserves further analysis.

Acknowledgements. We acknowledge funding from the French National Research Agency (ANR) under contract number ANR-18-CE31-0019 (SPLaSH). This paper includes data collected with the TESS mission, obtained from the

MAST data archive at the Space Telescope Science Institute (STScI). In particular, the TESS data secured in 2020 are part of the TESS Guest Investigator Programs G03263 (PI: P. Plavchan), G03141 (PI: E. Newton), and G03273 (PI: L. Vega). Together with other data and analyses of that particularly interesting system, that will be the subjects of forthcoming papers by Cale et al., Collins et al., El Mufti et al., Gilbert et al., Wittrock et al. Funding for the TESS mission is provided by the NASA Explorer Program. STScI is operated by the Association of Universities for Research in Astronomy, Inc., under NASA contract NAS 5-26555. We thank the TESS Team members for making available the extremely accurate photometric data they obtained. We acknowledge support by CFisUC projects (UIDB/04564/2020 and UIDP/04564/2020), GRAVITY (PTDC/FIS-AST/7002/2020), ENGAGE SKA (POCI-01-0145-FEDER-022217), and PHOBOS (POCI-01-0145-FEDER-029932), funded by COMPETE 2020 and FCT, Portugal. This work benefited from HPC resources of MesoPSL financed by the Region Ile de France and the project Equip@Meso (reference ANR-10-EQPX-29-01) of the programme Investissements d’Avenir.

References

- Augereau, J. C., Nelson, R. P., Lagrange, A. M., Papaloizou, J. C. B., & Mouillet, D. 2001, *A&A*, 370, 447
- Berdyugina, S. V. 2011, in *Astronomical Society of the Pacific Conference Series*, Vol. 437, *Solar Polarization 6*, ed. J. R. Kuhn, D. M. Harrington, H. Lin, S. V. Berdyugina, J. Trujillo-Bueno, S. L. Keil, & T. Rimmele, 219
- Bonfils, X., Delfosse, X., Udry, S., et al. 2013, *A&A*, 549, A109
- Claret, A. 2018, *A&A*, 618, A20
- Correia, A. C. M., Couetdic, J., Laskar, J., et al. 2010, *A&A*, 511, A21
- Correia, A. C. M., Udry, S., Mayor, M., et al. 2005, *A&A*, 440, 751
- Couetdic, J., Laskar, J., Correia, A. C. M., Mayor, M., & Udry, S. 2010, *A&A*, 519, A10
- Davenport, J. R. A., Hawley, S. L., Hebb, L., et al. 2014, *ApJ*, 797, 122
- Donati, J. F., Kouach, D., Moutou, C., et al. 2020, *MNRAS*, 498, 5684
- Farrés, A., Laskar, J., Blanes, S., et al. 2013, *Celestial Mechanics and Dynamical Astronomy*, 116, 141
- Foreman-Mackey, D., Hogg, D. W., Lang, D., & Goodman, J. 2013, *PASP*, 125, 306
- Gaia Collaboration. 2018, *VizieR Online Data Catalog*, I/345
- Hébrard, G., Díaz, R. F., Correia, A. C. M., et al. 2020, *A&A*, 640, A32
- Helled, R., Nettelmann, N., & Guillot, T. 2020, *Space Sci. Rev.*, 216, 38
- Heng, K. & Demory, B.-O. 2013, *ApJ*, 777, 100
- Hirano, T., Krishnamurthy, V., Gaidos, E., et al. 2020, *ApJ*, 899, L13
- Hsu, D. C., Ford, E. B., & Terrien, R. 2020, *MNRAS*, 498, 2249
- Kalas, P., Liu, M. C., & Matthews, B. C. 2004, *Science*, 303, 1990
- Klein, B., Donati, J.-F., Moutou, C., et al. 2020, *MNRAS*[arXiv:2011.13357]
- Kopparapu, R. K., Ramirez, R. M., SchottelKotte, J., et al. 2014, *ApJ*, 787, L29
- Kreidberg, L. 2015, *PASP*, 127, 1161
- Laskar, J. 1990, *Icarus*, 88, 266
- Laskar, J. 1993, *Physica D Nonlinear Phenomena*, 67, 257
- Lecavelier Des Etangs, A. 1998, *A&A*, 337, 501
- Lecavelier Des Etangs, A., Vidal-Madjar, A., & Ferlet, R. 1996, *A&A*, 307, 542
- Mamajek, E. E. & Bell, C. P. M. 2014, *MNRAS*, 445, 2169
- Martioli, E., Hébrard, G., Moutou, C., et al. 2020, *A&A*, 641, L1
- Palle, E., Oshagh, M., Casasayas-Barris, N., et al. 2020, *A&A*, 643, A25
- Plavchan, P., Barclay, T., Gagné, J., et al. 2020, *Nature*, 582, 497
- Rackham, B. V., Apai, D., & Giampapa, M. S. 2018, *ApJ*, 853, 122
- Ricker, G. R., Winn, J. N., Vanderspek, R., et al. 2015, *Journal of Astronomical Telescopes, Instruments, and Systems*, 1, 014003
- Robinson, R. D., Linsky, J. L., Woodgate, B. E., & Timothy, J. G. 2001, *ApJ*, 554, 368
- Stellingwerf, R. F. 1978, *ApJ*, 224, 953
- Tilley, M. A., Segura, A., Meadows, V., Hawley, S., & Davenport, J. 2019, *Astrobiology*, 19, 64
- Torres, C. A. O., Ferraz Mello, S., & Quast, G. R. 1972, *Astrophys. Lett.*, 11, 13
- White, R. J., Schaefer, G., Ten Brummelaar, T., et al. 2015, in *American Astronomical Society Meeting Abstracts*, Vol. 225, *American Astronomical Society Meeting Abstracts #225*, 348.12
- Wisniewski, J. P., Kowalski, A. F., Davenport, J. R. A., et al. 2019, *ApJ*, 883, L8

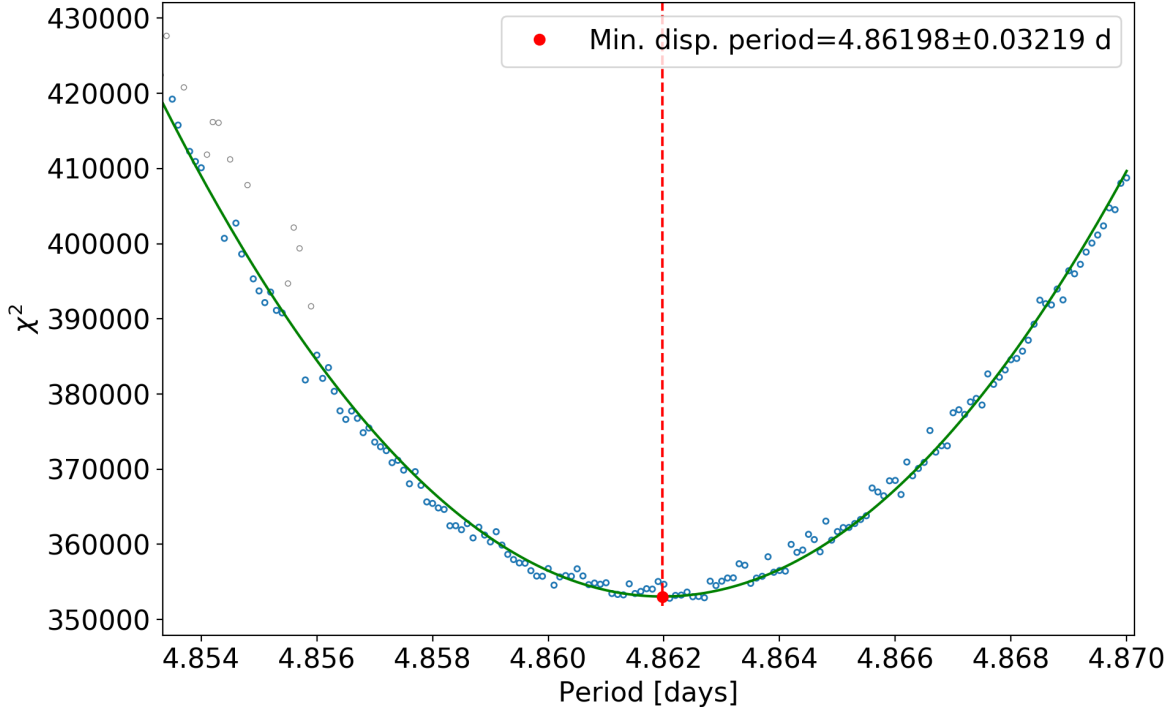


Fig. A.1. Rotation period versus chi-square for the reduced light curve of AU Mic after removing flares and planetary transits. Red dashed line shows the minimum χ^2 at $P = 4.862 \pm 0.032$ d obtained by a parabolic fit (green line).

Appendix A: Star rotation

In this appendix, we present an independent measurement of the star rotation period of AU Mic.

Starspots in AU Mic have a life time sufficiently large that the overall spot pattern did not change significantly during the 2018 TESS observations in the first visit. As one can see in the bottom panel of Fig. 1, there has been a more significant change in the spot pattern during the second visit of TESS, where the amplitude of the cyclic flux variations decreases with time. For this reason, we did not include the second visit data to measure the rotation period. Flares and planetary transits are removed from the original data using the models computed in Sects. 4, 5, and 6. We apply the phase dispersion minimization (PDM) method inspired by the work of Stellingwerf (1978), where we calculate the phase curve for several values of trial rotation periods ranging from 4.85 d to 4.88 d in steps of 0.0001 d. The rotation period of $P_r = 4.865$ d measured by Torres et al. (1972) was considered as initial guess to define our search range. For each trial period, we fit a cubic spline with 15 knots and calculate the chi-square by $\chi^2 = \sum (F_i - F_c)^2 / \sigma_i^2$, for F_i being the flux after removing flares and transits, F_c being the fit model, and σ_i being the flux uncertainty given by the TESS pipeline. The results are presented in Fig. A.1, where we find a minimum χ^2 at $P_r = 4.862 \pm 0.032$ d, which is consistent but less accurate than the rotation period of 4.863 ± 0.010 d obtained by Plavchan et al. (2020) from the same data set. The resulting phase curve and best fit model are presented in Fig. A.2. The final dispersion of residuals is $265 \text{ e}^- \text{ s}^{-1}$, which is more than twice the dispersion of residuals from the fit to the time series, that is, $99 \text{ e}^- \text{ s}^{-1}$ for the data from the first visit of TESS only. This discrepancy is likely due to the evolution or drifts of starspots during the several rotation cycles covered in the first visit and perhaps also due to differential rotation (Klein et al. 2020), which could generate a dispersion in the phase diagram since starspots at different latitudes are modulated by different periods.

Assuming the radius of AU Mic measured by interferometry of $R_\star = 0.75 \pm 0.03 R_\odot$ (White et al. 2015) and the rotation period of $P_r = 4.862 \pm 0.032$ d, we calculate the velocity at the equator as $v_{\text{eq}} = 2\pi R_\star / P_r = 7.8 \pm 0.3 \text{ km s}^{-1}$. This gives a maximum value of the projected velocity of $v_{\text{eq}} \sin(i_\star) < 8.1 \text{ km s}^{-1}$, for i_\star being the inclination angle of the rotation axis of the star with respect to the line of sight.

Appendix B: Flares fit parameters

Table B.1. Flares fit parameters.

Flare index	t_{peak} TBJD	amplitude $\text{e}^- \text{ s}^{-1}$	FWHM min
-------------	---------------------------	--	-------------

1	1325.5892	427.5	31.84
2	1325.7407	413.9	2.12
3	1326.1596	284.5	16.06
4	1326.2210	299.1	1.58
5	1326.3398	167.0	44.57
6	1326.3683	309.0	18.73
7	1326.5566	235.3	6.42
8	1326.6753	2121.5	20.65
9	1326.6978	2553.5	41.60
10	1326.7152	643.7	30.53
11	1326.8131	407.7	17.67
12	1327.1280	182.7	7.49
13	1327.2165	710.9	40.91
14	1327.3085	234.8	11.85
15	1327.4389	475.8	11.59
16	1327.4702	618.6	6.97
17	1327.5782	154.6	81.53
18	1327.8975	1430.4	8.48
19	1327.9450	405.8	100.61
20	1327.9970	259.6	35.31
21	1328.1461	537.6	10.28
22	1328.2454	323.7	7.80
23	1328.5056	7272.7	7.27
24	1328.7362	1838.0	3.24
25	1329.0420	301.9	17.15
26	1329.0900	378.9	14.88
27	1329.3240	689.1	13.58
28	1329.3803	2870.0	7.23
29	1329.4333	861.4	13.85
30	1329.4581	168.4	23.54
31	1330.0446	221.5	10.54
32	1330.1271	1112.7	25.56
33	1330.3750	338.9	36.00
34	1330.4089	295.2	5.27
35	1330.4475	184.4	71.83
36	1330.4524	1517.1	4.97
37	1330.6290	308.9	41.26
38	1330.8089	793.3	37.58
39	1330.9154	542.9	41.27
40	1331.3989	576.3	37.30
41	1331.4522	383.9	45.27
42	1331.8229	1486.5	3.80
43	1332.0069	178.2	20.97
44	1332.1019	195.6	23.99
45	1332.3460	536.7	9.86
46	1332.4868	371.5	105.57
47	1332.8700	299.1	12.73
48	1333.0207	504.1	6.85
49	1333.1734	617.6	22.72
50	1333.7962	288.6	36.04
51	1333.8896	5881.7	17.38
52	1333.8961	1535.9	9.14
53	1333.9019	1693.0	1.99
54	1334.1192	2089.1	13.44
55	1334.3769	811.2	5.82
56	1334.3925	442.6	5.83
57	1334.4750	172.1	61.01
58	1334.6162	527.2	9.53
59	1334.6378	223.0	8.21
60	1335.1163	11469.8	13.44
61	1335.1293	3267.2	11.25
62	1335.1639	1568.5	119.59
63	1335.3617	12798.6	5.00

64	1335.7034	3266.6	4.68
65	1335.7127	2214.6	0.65
66	1335.7684	206.0	16.34
67	1335.8508	202.2	17.09
68	1336.1992	434.9	20.97
69	1336.2313	1054.6	6.61
70	1336.2723	246.9	6.35
71	1336.3060	330.1	6.64
72	1336.5145	506.0	4.03
73	1336.5422	447.8	25.73
74	1336.6280	384.5	6.94
75	1336.9576	2572.0	9.42
76	1337.0216	1119.7	9.59
77	1337.0341	2277.9	21.60
78	1337.4779	681.6	8.05
79	1337.6259	473.3	3.50
80	1337.7419	355.1	16.21
81	1337.9638	346.6	18.35
82	1338.0760	215.2	4.12
83	1338.1343	190.1	7.34
84	1338.2252	1050.7	11.79
85	1338.2467	480.7	79.62
86	1338.4465	1526.2	2.42
87	1338.5024	1309.5	6.00
88	1338.5213	2095.5	18.37
89	1339.7341	200.4	9.29
90	1339.7816	466.4	34.29
91	1339.8383	1029.1	10.20
92	1340.5251	831.2	37.34
93	1340.6133	399.3	26.63
94	1340.9817	262.2	12.08
95	1341.3729	390.8	34.20
96	1341.9796	651.3	4.16
97	1342.1527	234.9	33.97
98	1342.1668	1938.2	0.72
99	1342.2354	224.3	12.48
100	1342.2719	209.6	18.33
101	1342.2962	365.4	1.86
102	1342.4018	122.2	39.11
103	1342.6043	421.3	4.31
104	1342.6336	255.9	24.70
105	1343.5102	1152.4	10.70
106	1343.9443	221.4	67.41
107	1344.0673	308.4	8.81
108	1344.2179	185.1	18.45
109	1344.5174	1246.6	3.87
110	1344.5350	699.4	11.15
111	1344.7107	272.2	88.42
112	1344.8182	782.1	18.63
113	1345.0144	474.4	14.07
114	1345.0717	405.8	3.72
115	1345.2198	425.1	23.96
116	1345.2599	296.4	23.24
117	1345.3944	2205.4	6.26
118	1345.4257	1232.8	24.61
119	1345.4816	329.7	24.13
120	1345.5112	1299.7	19.20
121	1345.5269	1908.0	31.64
122	1345.5806	512.1	39.17
123	1345.8324	526.4	3.90
124	1346.0371	756.7	11.13
125	1346.1915	1815.8	11.52
126	1346.2062	622.6	42.72
127	1346.2819	404.2	25.73

128	1346.4695	1355.0	0.72
129	1346.5211	5102.5	4.92
130	1346.5619	1014.5	9.39
131	1346.8081	311.1	21.61
132	1346.8791	221.4	2.58
133	1347.1743	224.4	49.74
134	1347.2600	436.4	7.55
135	1347.2696	773.2	7.27
136	1347.2753	319.5	8.28
137	1347.3391	491.7	2.12
138	1347.4334	396.3	9.55
139	1347.5908	326.9	19.73
140	1348.4951	445.8	42.47
141	1348.5686	479.9	7.37
142	1348.5951	55.8	0.01
143	1349.4535	1209.8	8.58
144	1349.8225	855.3	24.96
145	1350.0212	2444.4	23.85
146	1350.0812	1351.2	176.66
147	1350.1463	5308.9	4.98
148	1350.2853	1769.8	11.17
149	1350.2957	2460.0	12.99
150	1350.3062	588.5	10.67
151	1350.3212	392.3	7.01
152	1350.5975	595.6	18.42
153	1350.7887	347.2	4.36
154	1351.7021	258.3	49.28
155	1352.0038	254.4	59.49
156	1352.3524	1573.3	3.12
157	1352.6254	191.1	31.84
158	1352.7400	228.6	28.74
159	1352.9386	1629.7	0.43
160	1352.9528	486.5	18.27
161	1352.9878	437.3	49.39
162	1353.0282	250.0	13.94
163	2036.7060	1678.0	2.81
164	2036.9803	557.7	22.15
165	2037.0062	731.2	8.63
166	2037.0445	528.1	119.19
167	2037.4443	2482.4	5.59
168	2037.4926	529.0	6.16
169	2037.5567	629.3	0.58
170	2037.6398	455.7	1.57
171	2037.6661	285.1	0.07
172	2037.6752	11108.5	2.09
173	2037.6782	1725.8	10.30
174	2037.6794	2650.0	22.55
175	2037.7202	4475.7	3.33
176	2037.7460	313.6	9.43
177	2038.1988	160.4	44.15
178	2039.1836	4086.6	4.74
179	2039.2663	1637.8	1.89
180	2039.3501	3249.4	5.30
181	2039.3868	298.5	8.35
182	2039.4411	733.2	10.44
183	2039.5980	502.6	19.24
184	2039.8267	522.3	17.25
185	2039.8213	1015.2	3.54
186	2039.9915	538.1	176.11
187	2040.0245	560.2	20.59
188	2040.3473	403.2	1.96
189	2040.3548	313.3	2.82
190	2040.7923	594.5	20.55
191	2041.0997	231.1	53.67

192	2041.3700	871.5	3.82
193	2041.6072	409.8	9.48
194	2041.7500	118.8	33.72
195	2041.9375	333.8	45.71
196	2041.9876	387.4	56.35
197	2042.0502	407.3	19.53
198	2042.4858	5650.2	4.36
199	2042.5031	3220.7	8.76
200	2042.6066	532.7	8.93
201	2042.6998	522.8	1.64
202	2043.3819	228.0	2.52
203	2043.7737	266.4	48.63
204	2044.0924	532.7	13.80
205	2044.3488	540.4	3.00
206	2044.5147	371.3	30.05
207	2044.5761	600.4	34.88
208	2044.7252	313.4	33.65
209	2045.0332	163.6	8.18
210	2045.3312	610.8	2.30
211	2045.6075	242.5	24.26
212	2045.7409	408.9	3.56
213	2045.8442	351.2	34.24
214	2046.3703	316.6	24.52
215	2046.5418	284.7	95.80
216	2046.6323	682.6	40.90
217	2046.8676	806.2	2.98
218	2047.0374	191.9	6.36
219	2047.0975	270.8	8.22
220	2047.2069	184.4	0.04
221	2047.2155	3395.1	7.50
222	2047.2688	340.0	38.58
223	2047.3482	2740.9	9.52
224	2047.4462	891.1	48.97
225	2047.5051	1200.7	3.31
226	2047.5481	539.1	2.23
227	2047.6301	1138.6	9.53
228	2047.8328	1166.7	1.96
229	2048.0525	374.4	7.57
230	2049.2135	206.6	26.42
231	2049.5213	216.6	4.62
232	2049.7238	206.7	3.53
233	2049.7380	2365.4	2.16
234	2049.7424	274.2	13.64
235	2049.7546	468.5	8.35
236	2049.9163	84.0	182.42
237	2049.7972	280.8	4.41
238	2050.3662	460.2	11.07
239	2050.6606	453.6	18.94
240	2050.7854	309.4	36.35
241	2050.8613	1335.7	14.50
242	2050.9074	396.0	22.97
243	2051.1673	928.6	12.95
244	2051.1775	523.8	18.06
245	2051.4456	2285.7	10.79
246	2051.4575	1210.5	40.84
247	2051.5155	804.9	22.33
248	2051.5398	491.4	66.83
249	2051.8395	846.2	7.55
250	2052.2513	387.8	5.20
251	2052.3527	337.5	18.29
252	2052.6859	526.4	28.58
253	2052.8846	227.8	18.12
254	2053.0858	588.8	2.19
255	2053.2934	416.3	131.31

256	2053.4293	11831.0	3.11
257	2053.4313	4392.0	5.98
258	2053.4364	2771.1	21.72
259	2053.4471	1727.0	29.15
260	2053.5172	655.4	27.49
261	2053.7714	642.8	3.95
262	2053.8511	541.5	7.36
263	2054.2890	2125.9	40.06
264	2054.5200	247.5	416.71
265	2055.0243	356.7	25.01
266	2055.1195	139.0	16.47
267	2055.3076	305.4	3.46
268	2055.4149	370.8	10.58
269	2055.5277	365.8	9.81
270	2055.6639	278.9	66.80
271	2055.8219	257.3	34.42
272	2055.9072	1427.7	23.05
273	2055.9560	429.0	5.31
274	2056.2248	219.2	39.11
275	2056.2702	4218.7	1.21
276	2056.3009	648.6	22.67
277	2056.3696	432.8	39.37
278	2056.4690	416.0	38.42
279	2056.5167	515.0	15.28
280	2056.6882	814.3	3.02
281	2056.7114	411.5	3.34
282	2056.8307	3072.5	7.83
283	2056.8397	1642.1	23.47
284	2056.8744	556.6	35.16
285	2056.9135	5101.0	4.46
286	2056.9178	6950.3	21.77
287	2056.9413	1903.9	72.48
288	2057.0256	1115.2	165.60
289	2057.1330	855.9	7.08
290	2057.2076	727.6	10.93
291	2057.3293	335.9	1.80
292	2057.6220	176.0	15.67
293	2057.7999	8926.0	4.19
294	2057.8206	805.8	35.86
295	2058.0758	474.4	18.58
296	2058.1089	341.1	2.95
297	2058.2392	1637.1	10.08
298	2058.2417	1628.0	2.74
299	2058.2491	711.4	24.72
300	2058.2591	642.2	20.10
301	2058.2672	302.0	11.75
302	2058.3522	260.7	21.24
303	2058.7099	937.1	2.95
304	2058.7918	258.1	15.96
305	2058.8039	265.8	11.94
306	2058.8144	272.5	15.28
307	2058.8355	4984.7	0.16
308	2058.8387	3972.5	7.65
309	2058.8522	640.5	0.45
310	2058.9145	564.9	0.32
311	2058.9336	276.6	2.32
312	2058.9386	365.7	1.12
313	2059.0986	473.3	1.64
314	2059.1116	628.6	58.56
315	2059.3548	477.5	9.92
316	2059.3865	520.4	9.98
317	2059.4226	274.5	4.58
318	2059.5478	4219.3	1.21
319	2059.5512	3627.0	6.71

Table D.1. Fit transit parameters for an independent analysis of each of the three transit-like events identified as AU Mic c in the TESS light curve. The first row shows the previous results for Event 1 by Plavchan et al. (2020), the three following rows show the best fit parameters from our MCMC analysis of each event adopting an orbital period with an uniform prior of $P = \mathcal{U}(1, 500)$ d. The last three rows show the fit parameters using an orbital period with a normal prior of $P = \mathcal{N}(18.85895, 0.00003)$ d, as described in the text.

Event	T_0 [TBJD]	P [d]	a/R_\star	R_p/R_\star	i_p [°]	σ [ppm]
1 ^a	1342.22 ± 0.03	30 ± 6	40 ± 8	0.028 ± 0.006	89.28 ± 0.45	-
1	$1342.2247^{+0.0005}_{-0.0004}$	17^{+13}_{-8}	25^{+18}_{-11}	$0.036^{+0.0014}_{-0.0012}$	$88.6^{+0.9}_{-1.2}$	388
2	$2040.0063^{+0.0005}_{-0.0004}$	23^{+7}_{-5}	27 ± 6	$0.0420^{+0.0007}_{-0.0009}$	$88.28^{+0.3}_{-0.5}$	678
3	2058.8672 ± 0.0004	21^{+46}_{-12}	37^{+78}_{-21}	$0.0359^{+0.0009}_{-0.0005}$	$89.35^{+0.52}_{-1.03}$	646
1	$1342.2243^{+0.0004}_{-0.0006}$	$18.8574^{+0.0016}_{-0.0008}$	$31.3^{+0.4}_{-0.8}$	$0.0393^{+0.0005}_{-0.0004}$	$89.04^{+0.09}_{-0.06}$	355
2	2040.0062 ± 0.0003	$18.8588^{+0.00012}_{-0.00014}$	$23.8^{+1.5}_{-1.3}$	0.0444 ± 0.0007	88.2 ± 0.2	650
3	2058.8671 ± 0.0004	$18.8592^{+0.0002}_{-0.0003}$	$31.5^{+0.2}_{-2.1}$	0.0409 ± 0.0004	$89.03^{+0.07}_{-0.20}$	610

Notes. ^(a) Fit parameters for Event 1 obtained by Plavchan et al. (2020).

320	2059.6466	351.4	16.89
321	2059.6786	504.1	11.39
322	2060.2895	493.0	1.21
323	2060.4086	913.3	2.06
324	2060.5060	851.8	24.80

Appendix C: MCMC samples and posterior distributions

Appendix D: Independent fit to the transits of AU Mic c

This appendix presents the results obtained from an MCMC analysis (as in Sect. 5) performed on each transit of AU Mic c independently. D.1 shows the posterior of the transit parameters, where we present first the results using broad priors and then using the more restricted priors, as described in Sect. 6. We notice that the period and semi-major axis are not well constrained by the shape of the transits. As a consequence, when using broad priors, their posteriors turn out to have relatively large uncertainties. However, the posterior of all parameters agree within 3σ among the three events and they also agree with our derived period of $P \sim 18.86$ -d. The fit parameters for the more constrained priors also agree within 3σ , and the dispersion of residuals are improved with respect to the unconstrained solution, which supports our hypothesis that these events are caused by the transits of the same planet, namely, AU Mic c.

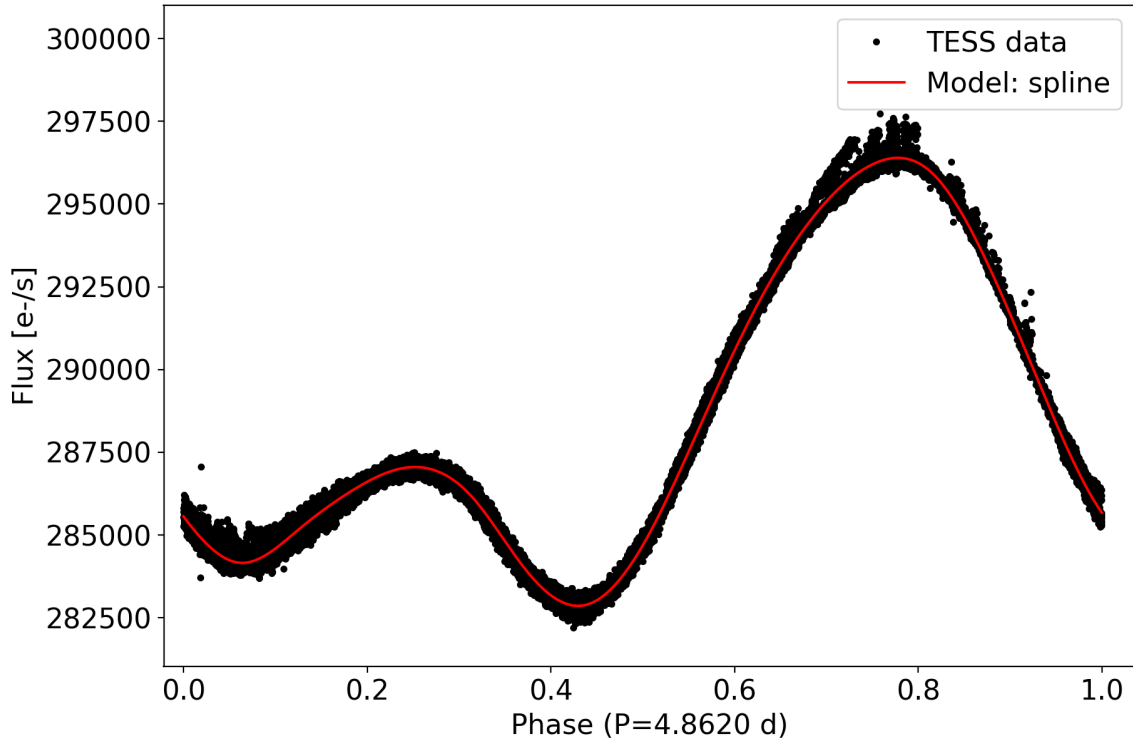


Fig. A.2. Phased light curve of AU Mic using our measured rotation period of 4.862 d. Black points show the 2018 TESS (first visit only) fluxes after removing the flares and transits best fit models, and red line shows the best fit cubic spline model to the phased data.

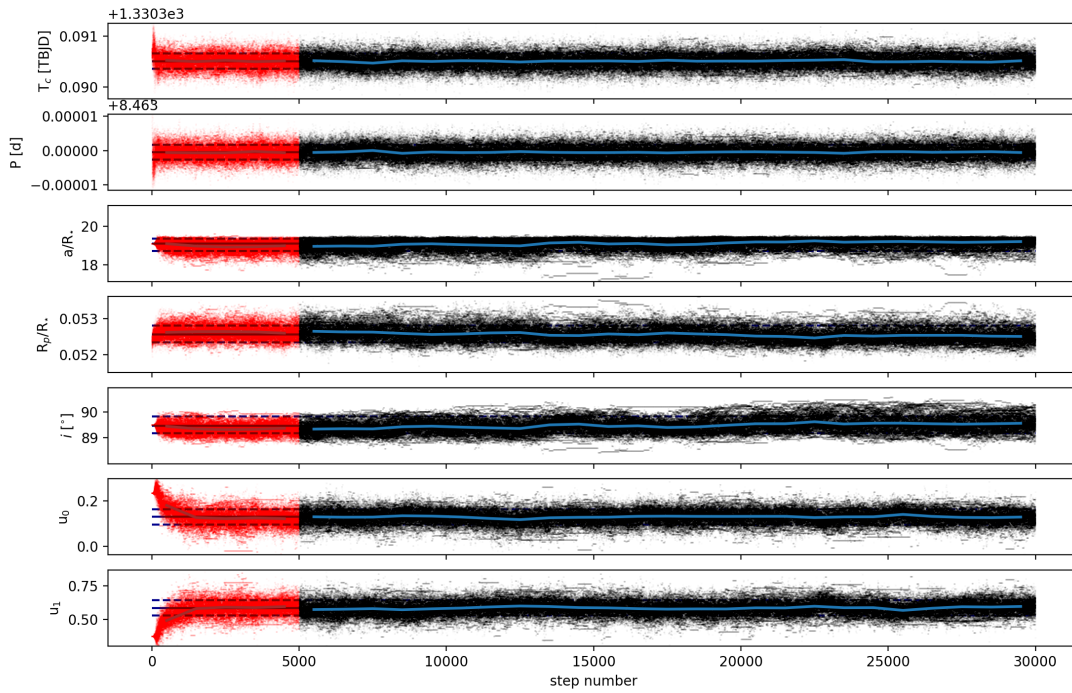


Fig. C.1. MCMC samples (black dots) used to calculate the posterior distributions of the transit parameters of AU Mic b. The red dots show the discarded samples corresponding to the first 5000 steps of the chain. The blue lines show the median calculated for bins of 1000 steps. Dashed lines show the 16- and 84-percentiles and the solid horizontal lines shows the medians of the valid samples.)

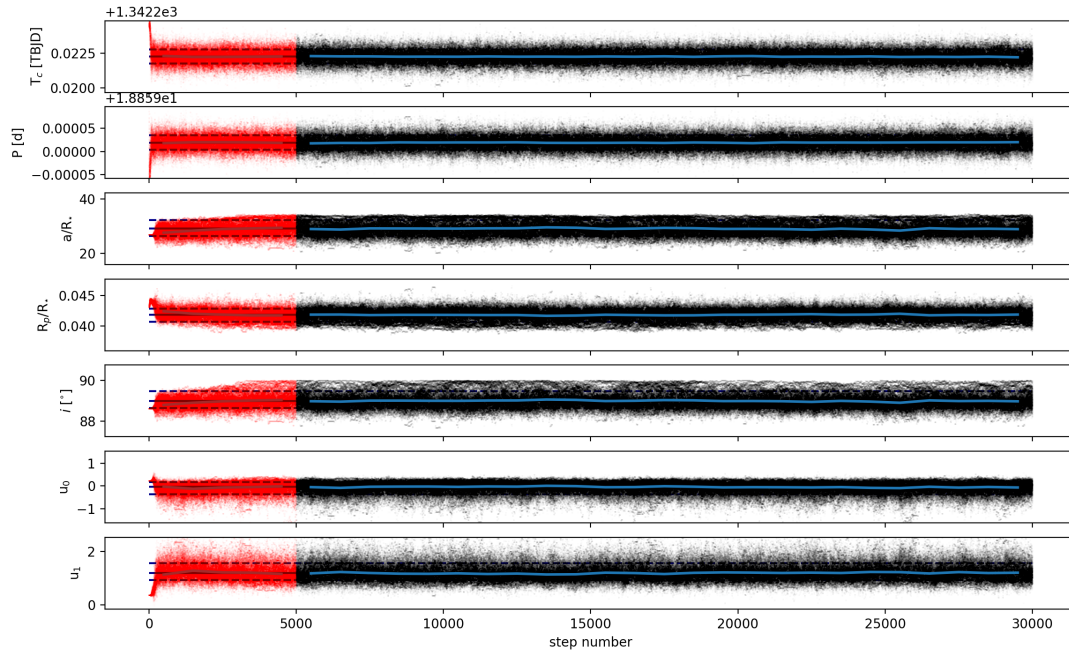


Fig. C.2. Same Fig. C.1 for the MCMC samples of the transit parameters of AU Mic c.

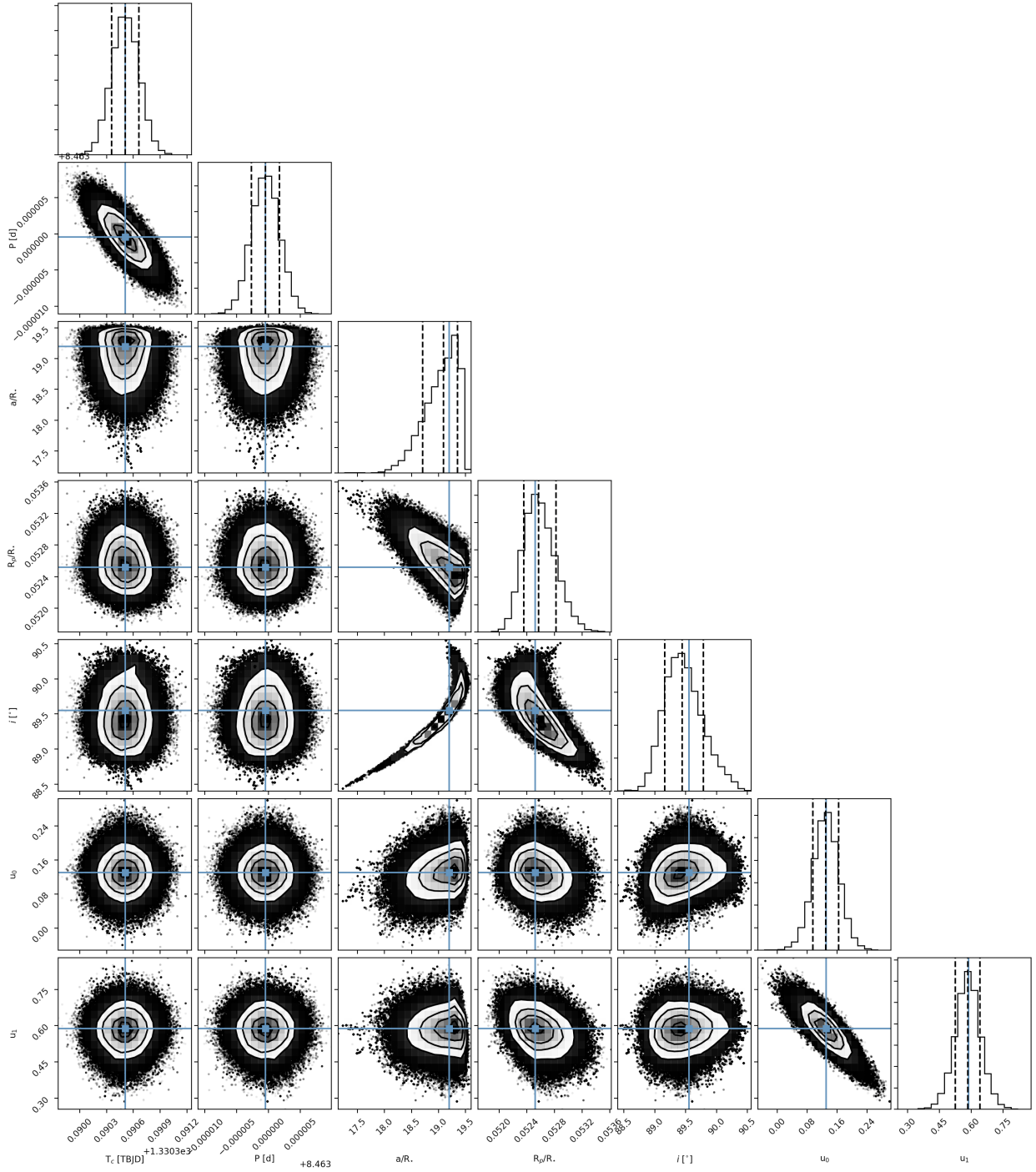


Fig. C.3. Pairs plot showing the MCMC samples and posterior distributions for the transit parameters of AU Mic b as presented in Table 2. The contours mark the 1σ , 2σ , and 3σ regions of the distribution. The blue crosses indicate the best fit values for each parameter and the dashed vertical lines in the projected distributions show the median values and the 1σ uncertainty (34% on each side of the median).

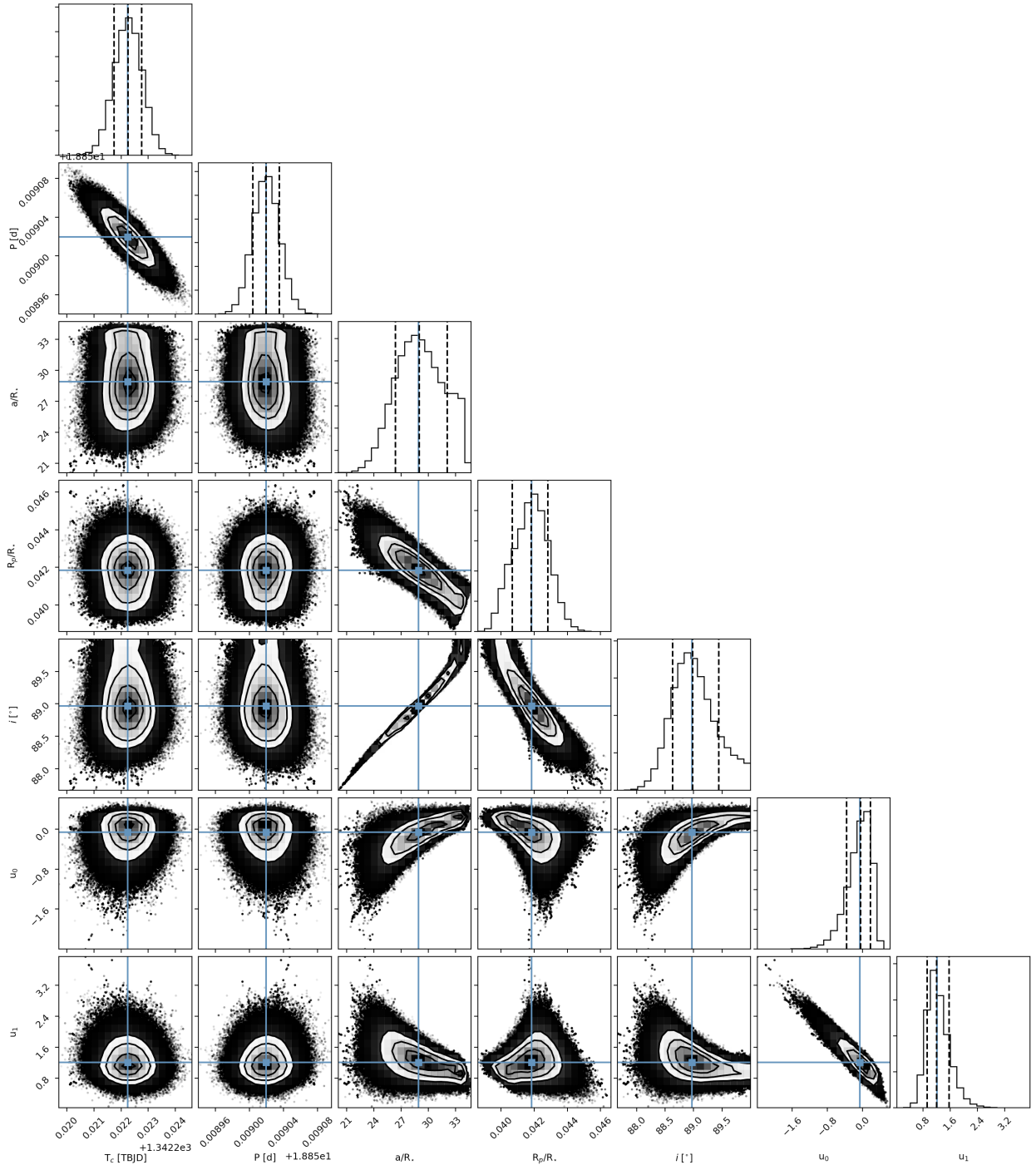


Fig. C.4. Pairs plot showing the MCMC samples and posterior distributions for the transit parameters of AU Mic b as presented in Table 2. Details are the same as in Fig. C.3 for the analysis of the three transits of AU Mic c.